Journal of Materials Chemistry A

PAPER

View Article Online
View Journal | View Issue

Cite this: J. Mater. Chem. A, 2014, 2, 13655

Highly sensitive SnO_2 nanofiber chemiresistors with a low optimal operating temperature: synergistic effect of Cu^{2+}/Au co-doping†

Zhenyu Li,[ab] Xungai Wang[a] and Tong Lin*[a]

Received 18th April 2014
Accepted 23rd June 2014

DOI: 10.1039/c4ta01926a

www.rsc.org/MaterialsA

Metal oxide chemiresistors (MOCs) with a low optimal operating temperature, high sensitivity and fast response/recovery are highly promising for various applications, but remain challenging to realize. Herein, we demonstrate that SnO_2 nanofibers after being co-doped with Cu^{2+} and Au show considerably enhanced sensing performances at an unexpectedly decreased operating temperature. A synergistic effect occurs when the two dopants are introduced together. Co-doping may form a novel strategy to the development of ultrasensitive MOCs working at a low optimal temperature.

Introduction

Metal oxide chemiresistors (MOCs), which can monitor gas or vapor based on resistance change, often have high sensitivity, low cost and compatibility with microelectronic processing. They show promising applications in environmental, health, security and automotive sectors.[1–5] MOCs from a nanostructured metal oxide are of particular interest because the large surface-to-volume ratio allows the exposure of as many sensing sites as possible on the surface, offering cutting-edge sensing ability (*e.g.* rapid adsorption/desorption).[6–17] Most of the MOCs, however, have to work at a temperature typically above 200 °C, which consumes a large amount of energy. During working at a high temperature the oxide grains may coalesce, which is detrimental to the sensing performance. The high working temperature also confines the use of MOCs for detection of explosives.[11]

Efforts to lower the operating temperature of MOCs have been reported by several groups. Approaches include improving the conductivity of metal oxides, increasing the amount of ionosorbed oxygen species on the metal oxide surface, or enhancing interactions between target molecules and ionosorbed oxygen species of the metal oxide. For example, carbon nanotubes[18–21] or graphene[22–26] were added to improve the conductivity of metal oxides at a low temperature and non-stoichiometric metal oxides were employed to increase the ionosorbed oxygen species on the oxide surface.[27–30] UV-light irradiation was also reported to reduce the MOC operating temperature because UV-light irradiation could increase not only the conductivity of metal oxides but also the ionosorbed oxygen species on the metal oxide.[31–35] Despite the success in lowering the operating temperature, the MOCs reported often had low response and recovery speeds (*e.g.* larger than 1 min), which were attributed to weak interactions between target molecules and metal oxide, leading to inevitable delay in monitoring of target states.

Doping a metal oxide with a noble metal, such as Au, is an effective route to reduce the activation energy (E_a) of the reaction between target molecules and ionosorbed oxygen species,[36] which has been widely used to enhance the sensing performance of MOCs.[37–40] Nevertheless, Au doping normally shows a finite change in the MOC operating temperature. In contrast, doping with an extrinsic metal ion was reported to considerably increase ionosorbed oxygen species on the metal oxide surface, which is derived from the increased oxygen vacancies in the host crystals because of the mismatch between the two metal ions.[41–43] However, whether co-doping with both an extrinsic metal ion and noble metal can increase the sensitivity but decrease the optimal operating temperature of a MOC has not been reported in the research literature.

Herein, we demonstrate a novel strategy to increase the MOC sensitivity and meanwhile lower the optimal operating temperature by co-doping a metal oxide with metal ions and noble metal. Electrospinning was employed to prepare SnO_2 nanofibers containing both Cu^{2+} and Au. The Cu^{2+}/Au co-doped SnO_2 nanofiber MOCs had an optimal operating temperature (160 °C) to detect acetylene (C_2H_2), almost 100 °C lower than those made of pristine SnO_2 nanofibers or SnO_2 nanofibers just doped with Cu^{2+} or Au. The co-doping caused a synergistic effect which considerably enhanced the sensitivity. Acetylene is selected because it is often generated in oil-filled power equipment, such as large power transformers. The detection of C_2H_2

[a]Institute for Frontier Materials, Deakin University, Geelong, Victoria 3216, Australia. E-mail: tong.lin@deakin.edu.au; Tel: +61 3 52271245

[b]Alan G. MacDiarmid Institute, Jilin University, Changchun 130012, P. R. China

† Electronic supplementary information (ESI) available: Details of SEM and TEM images, comparison between different MOCs against C_2H_2, XRD patterns, and SnO_2 grain size. See DOI: 10.1039/c4ta01926a

gas is important for on-site monitoring of the working state and diagnosing the faults of oil-filled power equipment.

Experimental

Materials

$SnCl_2 \cdot 2H_2O$ was acquired from Tianjin Chemical Co. and $Cu(NO_3)_2 \cdot 3H_2O$ was from Beijing Chemical Co. Ethanol, *N*,*N*′-dimethylformamide (DMF), poly(vinyl pyrrolidone) (PVP, $M_w = 1\ 300\ 000$) and gold(III) chloride trihydrate were obtained from Aldrich. All materials were used as received. The solution for electrospinning was prepared by dissolving $SnCl_2 \cdot 2H_2O$ (0.4 g) in a solvent mixture of DMF (4.4 g) and ethanol (4.4 g) under vigorous stirring. PVP (0.8 g), $Cu(NO_3)_2 \cdot 3H_2O$ and gold(III) chloride trihydrate were then added into the solution, and a homogeneous solution was formed by further stirring vigorously for 30 min. The Au/Sn atomic ratio in the solution was kept at 5 : 100 and the Cu/Sn atomic ratio was controlled at 1 : 100, 2 : 100, and 3 : 100. For comparison, solutions without containing elements Cu and Au were also prepared using the same procedure.

Preparation of nanofibers

Precursor nanofibers were prepared using a purpose-made electrospinning setup consisting of a high voltage power supply, a glass syringe (inner diameter, 1 mm) and a metal plate collector. The solution prepared was placed into the syringe. A high DC voltage (15 kV) was then applied between the syringe needle tip and the collector (distance 20 cm). Fibers were electrospun from the syringe needle and deposited onto the collector. After electrospinning, the precursor fibers were peeled off the collector and then calcined at 600 °C in air for 5 hours.

Fabrication of MOC sensor devices

The nanofibers prepared were mixed with deionized water at a fiber–water ratio of 100 : 15 (wt/wt) and the mixture was ground into a paste, which was spin-coated onto a ceramic tube on which a pair of gold electrodes was pre-printed. A Pt heating wire was inserted into the tube to form a side-heated gas sensor. The sensor device was dried for 2 days at room temperature. Prior to the gas sensing measurement, all the MOC devices (nanofibers with ceramic tubes) were aged at 350 °C for 12 h. During the measurement, all the devices were stabilized at each testing temperature for at least 6 h.

Characterization of sensor properties

Sensing properties were measured using a static flow system, which was composed of a heater, a gas distributor and a data acquisition system. Resistance change was recorded during the exposure of the sensor device to C_2H_2-containing air, using a CGS-8 intelligent test system (Beijing Elite Tech Co. Ltd, China). When the response reached a constant value, the device was then recovered by exposing to pure air. The gas sensor response (R_a/R_g) was defined as the device resistance ratio in air (R_a) and in testing gas (R_g).[44] The test was performed in a temperature range of 120 °C–300 °C. The response time was defined as the time taken by the sensor device to achieve 90% change of the resistance during exposure to the test gas, while the recovery time was defined as the time required for recovery of 90% resistance in pure air.[45]

Other characterization

The morphologies and structures of the samples were investigated by transmission electron microscopy (TEM) on a JEOL-2100 with an acceleration voltage of 200 kV and a scanning electron microscope (SEM Supra 55VP). Crystal structures were studied by X-ray diffraction (XRD, Scintag XDS 2000 diffractometer with Cu Kα radiation). X-ray photoelectron spectra (XPS) were recorded on an ESCLAB MKII using Al as the excitation source. All peaks in the XPS survey spectrum were calibrated based on the binding energy of C 1s (284.6 eV). Surface area was measured using the BET nitrogen adsorption method on a Micromeritics ASAP2000. The pore size distribution was derived by the Barrett–Joyner–Halenda method. To measure the electrical resistance of the SnO_2 nanofiber sample, a pair of gold electrodes (thickness 100 nm) with 60 μm channel spacing was evaporated onto a SiO_2 wafer. The nanofiber sample (1 mg) was dispersed in 200 μL distilled water. After ultrasonication for 2 minutes, 10 μL nanofiber dispersion was added dropwise into the channel spacing, and the electrode was finally dried.

Results and discussion

Morphology and crystalline structure

Cu/Au co-doped SnO_2 nanofibers (CASNFs) were prepared by electrospinning of a PVP solution containing $SnCl_2$, $Cu(NO_3)_2$ and gold(III) chloride to get precursor nanofibers and by subsequent calcination of the precursor nanofibers at 600 °C in air to remove the polymer component and form a SnO_2 crystal

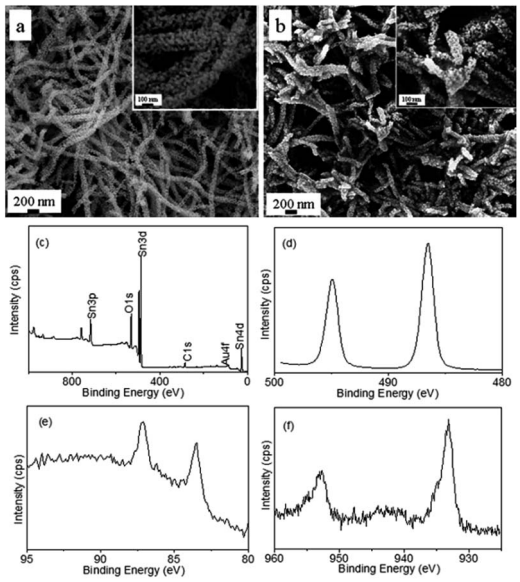

Fig. 1 SEM images of (a) CASNFs and (b) pristine SnO_2 nanofibers, (c) XPS survey spectrum; high resolution XPS (d) Sn 3d, (e) Au 4f, and (f) Cu 2p spectra. (CASNFs for b–f based on 1Cu/5Au/SnO_2.)

phase. Fig. 1a shows the typical SEM image of the CASNFs (molar ratio of Cu/Au/Sn is 1 : 5 : 100, also referred to as 1Cu/5Au/SnO_2), indicating a porous structure with lots of micro-pores between the adjacent CASNFs. Nano-pores among the agglomerated gains throughout the CASNFs can be clearly seen from the higher magnification image (inset of Fig. 1a). For comparison, the SEM images of pristine SnO_2 nanofibers without Au and Cu, prepared by the same method, are presented in Fig. 1b. The pristine SnO_2 nanofibers showed a similar morphology to CASNFs. A variation of the Cu/Sn ratio in CASNFs was found to have little effect on the fiber morphology (see ESI†).

The formation of porous nanofibers was derived from removal of the PVP component from the fibers and crystallization of metal oxides, which was similar to other metal oxide nanofibers prepared by an electrospinning route.[46] The porous fiber structure is preferable to the absorption of target molecules for gas detection.[36]

X-ray photoelectron spectroscopy (XPS) was used to examine the surface chemical component of CASNFs. Fig. 1c shows the survey spectrum of CASNFs (1Cu/5Au/SnO_2), indicating the existence of elements Sn, C, Au, Cu and O on the nanofiber surface. The high resolution XPS Sn 3d spectrum in Fig. 1d shows two symmetric peaks with binding energies at 494.9 eV and 486.4 eV, which are assigned to Sn $3d_{3/2}$ and Sn $3d_{5/2}$. The well separated spin–orbit components between the two peaks (Δ_{metal} = 8.5 eV) indicated that the element Sn was in the Sn^{4+} state.[47] The high resolution Au 4f spectrum showed two peaks at 83.4 eV and 87.8 eV, corresponding to Au $4f_{7/2}$ and Au $4f_{5/2}$, respectively (Fig. 1e). Since no peaks were located at around 85.5 eV and 86.3 eV, which are the characteristic binding energies of oxidized Au, Au in CASNFs was in the metallic state. In contrast to bulk metallic Au (84.1 eV), the Au in nanofibers had a negative shift (−0.7 eV) in binding energy. This indicates strong interaction between Au and SnO_2 (*e.g.* electron transfer from SnO_2 to Au (ref. 15)). For element Cu, the $2p_{3/2}$ and $2p_{1/2}$ peaks were detected at 932.1 eV and 952.0 eV (Fig. 1f). The satellite peak at higher binding energy confirms that the chemical state of Cu ions is Cu^{2+} in the final products.[48]

Fig. 2 shows the XRD patterns of SnO_2 nanofibers. SnO_2 in CASNFs had the characteristics of the tetragonal rutile SnO_2 crystal phase (JCPDS 41-1445), while Au was in the face centered cubic crystal phase (JCPDS no. 65-2870). Since no peaks associated with the copper oxide phase were detected, a long order CuO lattice was not formed in the CASNFs.

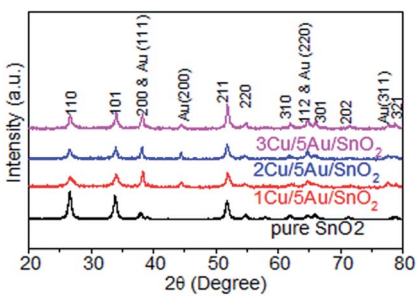

Fig. 2 XRD patterns of CASNFs and pure SnO_2 nanofibers.

Au and Cu^{2+} in SnO_2 nanofibers were examined by a TEM EDS mapping technique (see the images in the ESI†). It was interesting to note that Au existed in the form of particles scattering in the nanofibers, while element Cu distributed throughout the entire nanofibers. Despite the dispersion state, "doping" here was still used to specify the effect of Cu^{2+} ions and Au nanoparticles on SnO_2 nanofibers.

High-resolution XRD was employed to examine the effect of Cu^{2+} on SnO_2 in the Au crystal phase. The SnO_2 (101) peak was found to slightly shift to a lower angle when increasing the Cu^{2+} doping level from 1 at% to 2 at% (see ESI†). Such a shift was attributed to a substitution mechanism upon incorporation of Cu^{2+} ions into the SnO_2 lattice network.[49] When the Cu^{2+}-doping level was further increased to 3 at%, the peak recovered a little, indicating saturation of the Cu^{2+} substitution in the SnO_2 crystal.

By comparing the XRD patterns of 5Au/SnO_2 and 1Cu/5Au/SnO_2, we noted that the presence of Cu^{2+} ions in the Au-doped SnO_2 nanofibres led to an increase of the peak at $2\theta = 38°$, which corresponded to the Au (111) crystal phase. The peak was higher than that of SnO_2 (110) and SnO_2 (101). For the SnO_2 nanofibers just doped with Au (*i.e.* 5Au/SnO_2), however, the Au (111) peak was lower than that of SnO_2 (110) and SnO_2 (101) (see ESI†). In addition, Au-doping did not affect the peaks of SnO_2 (200). These results suggest that Cu^{2+}-doping facilitates the growth of the Au (111) crystal phase, leading to an increase in the catalytic ability.

Sensing properties

Sensing properties against C_2H_2 were studied. Fig. 3a shows the gas sensor response (R_a/R_g) of the MOC devices in 100 ppm C_2H_2 at different operating temperatures. For pristine SnO_2, the response value increased with increasing operating temperature up to 260 °C. Further increasing the temperature led to a

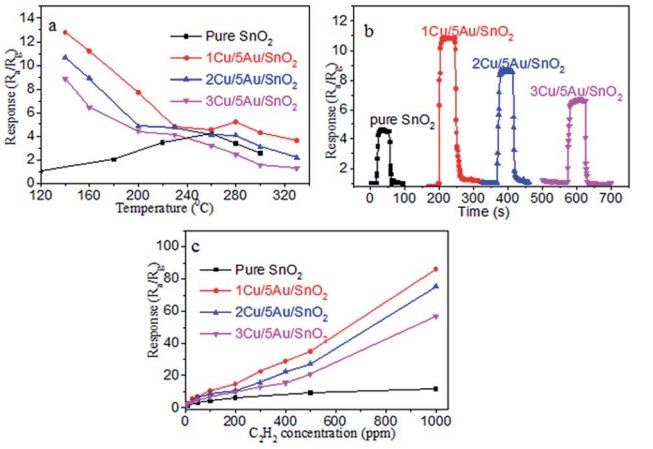

Fig. 3 (a) Sensor response of MOC devices as a function of operating temperature (C_2H_2 concentration, 100 ppm), (b) response/recovery curves of MOC devices against 100 ppm C_2H_2, (c) effect of the C_2H_2 concentration on the sensor response (in b and c, the working temperature for the pristine SnO_2 nanofiber and CASNFs was 260 °C and 160 °C, respectively).

decrease in the response value.[36] The response and recovery curve of the device in 100 ppm C_2H_2 at 260 °C is shown in Fig. 3b. The response time and recovery time were both ~7 s. Therefore, the optimal operating temperature of the pristine SnO_2 nanofiber MOC was 260 °C.

For CASNF-based MOC devices, the response value decayed monotonically when the operating temperature increased from 140 °C to 320 °C. Here, 140 °C was selected as the lower limit of operating temperature for the reason that the device resistance became too large to be measured by the test system when the temperature was below this point. Among the CASNF devices, the one from 1Cu/5Au/SnO_2 had the highest response value. We also found that at 140 °C, CASNF MOCs exhibited long response/recovery behaviors, which could not be used to effectively monitor target molecules. When the working temperature reached 160 °C, the devices showed good response/recovery behavior. The response and recovery curves of the CASNF devices in 100 ppm C_2H_2 at 160 °C are shown in Fig. 3b. The response/recovery behaviors for CASNF devices were 5 s/13 s, 7 s/6 s, and 7 s/6 s for 1Cu/5Au/SnO_2, 2Cu/5Au/SnO_2, and 3Cu/5Au/SnO_2, respectively. Therefore, 160 °C was identified to be the optimal operating temperature of the CASNFs. The effect of the C_2H_2 concentration on the response of MOCs is shown in Fig. 3c. At the optimal operating temperature, CASNF devices had higher response than pristine SnO_2 nanofiber devices, although the former worked at a temperature 100 °C lower than the latter.

We also quantitatively compared our results on sensing performances with those reported by researchers on MOCs for monitoring C_2H_2 (see ESI†). It is clearly indicated that our CASNF MOCs exhibit better sensing performance than those reported in previous reports.

To explore the role of Cu^{2+}/Au co-doping in the enhancement of sensing performances, SnO_2 nanofibers containing just one dopant were prepared using the same method, and the fiber morphology, crystalline structure, and sensing performance were examined. SnO_2 nanofibers doped with Cu^{2+} or Au showed a similar fiber morphology to CASNFs (see ESI†). The single dopant had little effect on the fiber diameter. The XRD curves also confirmed that the dopants did not change the tetragonal rutile crystal characteristics of SnO_2 (JCPDS 41-1445) (see ESI†).

Fig. 4a shows the gas response of MOC devices made of SnO_2 nanofibers doped with Cu^{2+} or Au. In 100 ppm C_2H_2, the Cu^{2+} doped SnO_2 showed a similar response trend to the pristine SnO_2 nanofiber device. Cu^{2+}-doping did not change the optimal operating temperature, but increased the response value and response/recovery behaviors (Fig. 4b).

For the Au-doped SnO_2 nanofibers, the MOC device had an optimal operating temperature of 220 °C, which was slightly lower than that of pristine SnO_2 nanofibers (260 °C), but higher than that of CASNFs (160 °C). The response and recovery times of Au-doped devices are 6 s and 7 s (Fig. 4b). The slightly decreased optimal operating temperature was explained by the spill-over and electronic (chemistry) sensitization of Au.[50–52]

The above sensing results clearly indicate that the co-doped SnO_2 nanofibers have a much higher MOC response value than those just doped with single Cu^{2+} or single Au. A synergistic

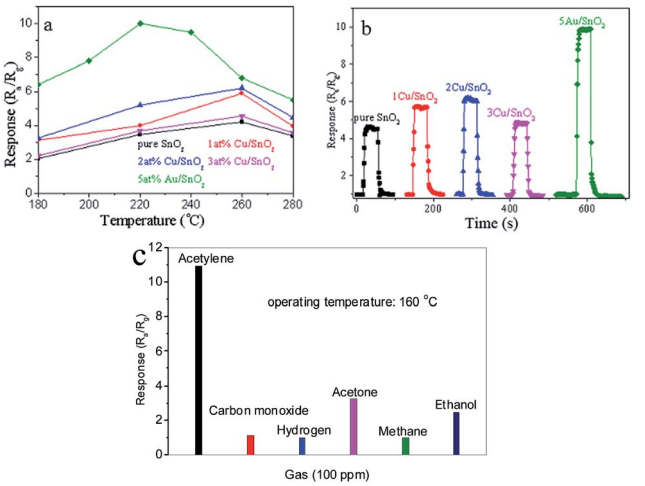

Fig. 4 (a) MOC sensitivity of SnO_2 nanofibers doped with Cu^{2+} or Au (in 100 ppm C_2H_2), (b) response/recovery curves of the MOC devices against 100 ppm C_2H_2 (the operating temperature was 260 °C for the Cu^{2+}-doped SnO_2, and 220 °C for the Au-doped SnO_2), (c) cross-response of the MOC device (1Cu/5Au/SnO_2).

effect on the gas response occurs when SnO_2 nanofibers are co-2doped with Cu^{2+} and Au.

We also tested the cross-response of our MOC device (1Cu/5Au/SnO_2) to different gases, including carbon monoxide, hydrogen, acetone, methane and ethanol. As shown in Fig. 4c, the MOC device has a good sensing selectivity to acetylene.

To find out the source of the synergetic effect, we also measured the effect of Cu^{2+} and Au on the electrical resistance, surface area and pore size of SnO_2 nanofibers. For pure SnO_2 nanofibers, the resistance measured by a two-probe method was 70 kΩ. Doping SnO_2 with Au or Cu considerably increased the resistance, respectively to 4×10^5 kΩ (Au 5 at%) and 2×10^5 kΩ (Cu 2 at%). Co-doping further increased the resistance. The resistance of Cu^{2+}/Au co-doped SnO_2 nanofibers (1Cu/5Au/SnO_2) was too large to be measured by our test system.

The BET surface area of all nanofiber samples is listed in Table 1 (see the detailed results in the ESI†). Cu^{2+}-doping increased the surface area, while Au-doping led to a reverse trend. Co-doped SnO_2 nanofibers showed a slightly lower surface area than the pure SnO_2 nanofibers.

The pores in the nanofiber samples showed a bimodal and wide size distribution (see ESI†). Here, the pore size values centered in the bimodal distribution are also listed in Table 1. Doping with Cu^{2+} increased the size of smaller pores, but decreased the size of the larger pores. Au-doping showed a

Table 1 BET surface area and pore size

Samples	Surface area ($m^2\ g^{-1}$)	Pore size 1 (nm)	Pore size 2 (nm)
Pure SnO_2	33.3	1.7	21.8
5Au/SnO_2	30.5	1.5	25.9
2Cu/SnO_2	64.8	2.1	20.4
1Cu/5Au/SnO_2	32.0	1.6	20.7

reverse change. When SnO_2 was co-doped with Au and Cu^{2+}, both the large and small pores were slightly reduced when compared with those in the pure SnO_2 nanofiber sample.

Discussion

With using n-type semiconducting metal oxides as a sensor medium, oxygen vacancies play a critical role in determining the sensing performance. To approach the stoichiometry of metal oxide, oxygen molecules are absorbed on the surface. The oxygen species act as an electron acceptor to withdraw electrons from the conduction band of the metal oxides. Ionosorbed oxygen species are thus formed, resulting in an electron-depleted surface region (also called the "space-charge layer") and increase in electrical resistance. The ionosorbed oxygen species are reverted when exposed to reducing gas. In this way, the electrons trapped by the oxygen species feed back to the metal oxides, leading to a decrease in the resistance. In our case, the reaction between C_2H_2 and the ionosorbed oxygen species on SnO_2 is shown in eqn (1).

$$C_2H_2 + 5O_{ads}^- \rightarrow 2CO_2 + H_2O + 5e^- \quad (1)$$

The reaction coefficient (α) is governed by several factors and can be expressed as:[36]

$$\alpha = \alpha_0 \exp\left(-\frac{E_a}{RT}\right) \quad (2)$$

where E_a is the activation energy of the reaction, α_0 is the pre-exponential constant, T is the reaction temperature and R is the gas constant.

Introducing Au nanoparticles into SnO_2 nanofibers could lead to three scenarios: (1) reduction of E_a owing to the catalytic effect of Au, which improves the reaction efficiency at a low temperature; (2) increasing the amount of ionosorbed oxygen species on SnO_2,[52] thus strengthening the interactions between C_2H_2 and the ionosorbed oxygen species and hence increasing the sensitivity; (3) increasing the height of the space-charge layer, which also leads to enhanced sensitivity. The last scenario comes from the band structure. Since the working function of Au is typically lower than the Fermi level of SnO_2, a Schottky barrier forms at the Au–SnO_2 interface and electrons transfer from SnO_2 to Au.[53]

When SnO_2 is doped with Cu^{2+}, the grain size of SnO_2 decreases because of the mismatched atomic radius between Cu^{2+} (74 pm) and Sn^{4+} (69 pm). The effect of the Cu/Sn atomic ratio on the grain size of SnO_2 in the nanofibers is shown in the ESI†, which is similar to a previous report.[54] The reduction in the SnO_2 grain size allows more active sites on the surface, which gives higher gas sensitivity.

The synergetic effect of Cu^{2+}/Au co-doping was proposed. Cu^{2+} doping increases the active sites on the SnO_2 surface owing to the reduced SnO_2 grain size. Au nanoparticles in SnO_2 nanofibers also enhance the sensitivity. Since the presence of Cu^{2+} in the Au-doped SnO_2 nanofiber system also increases the Au (111) crystal phase, the catalytic ability against acetylene is further enhanced considerably. As a result, MOC devices show increased sensing performance at a reduced optimal operating temperature.

For Cu^{2+}/Au co-doped SnO_2 MOC devices, the monotonous decrease of gas response with increasing sensor temperature can be explained by the increased Au (111) phase and the electrical resistance of Cu^{2+}/Au co-doped SnO_2 nanofibers.

Conclusions

A simple route to lower the working temperature and meanwhile increase the sensitivity of MOCs has been developed based on Cu^{2+}/Au co-doped SnO_2 nanofibers. A synergistic effect was found between Cu^{2+} and Au, making the co-doped nanofibers have an unexpectedly high gas sensitivity at a low optimal working temperature. Co-doping may form a novel strategy to the development of ultrasensitive MOCs with a low optimal working temperature.

References

1 G. Eranna, B. C. Joshi, D. P. Runthala and R. P. Gupta, *Crit. Rev. Solid State Mater. Sci.*, 2004, **29**, 111–188.
2 M. Batzill and U. Diebold, *Prog. Surf. Sci.*, 2005, **79**, 47–154.
3 M. E. Franke, T. J. Koplin and U. Simon, *Small*, 2006, **2**, 36–50.
4 N. Barsan, D. Koziej and U. Weimar, *Sens. Actuators, B*, 2007, **121**, 18–35.
5 G. Korotcenkov, *Mater. Sci. Eng., B*, 2007, **139**, 1–23.
6 N. Barsan, M. Schweizer-Berberich and W. Gopel, *Fresenius' J. Anal. Chem.*, 1999, **365**, 287–304.
7 A. Kolmakov and M. Moskovits, *Annu. Rev. Mater. Res.*, 2004, **34**, 151–180.
8 A. Rothschild and Y. Komem, *J. Appl. Phys.*, 2004, **95**, 6374–6380.
9 D. H. Zhang, Z. Q. Liu, C. Li, T. Tang, X. L. Liu, S. Han, B. Lei and C. W. Zhou, *Nano Lett.*, 2004, **4**, 1919–1924.
10 A. Kolmakov, D. O. Klenov, Y. Lilach, S. Stemmer and M. Moskovits, *Nano Lett.*, 2005, **5**, 667–673.
11 E. Comini, *Anal. Chim. Acta*, 2006, **568**, 28–40.
12 I. D. Kim, A. Rothschild, B. H. Lee, D. Y. Kim, S. M. Jo and H. L. Tuller, *Nano Lett.*, 2006, **6**, 2009–2013.
13 M. Paulose, O. K. Varghese, G. K. Mor, C. A. Grimes and K. G. Ong, *Nanotechnology*, 2006, **17**, 398–402.
14 G. Korotcenkov, *Mater. Sci. Eng., R*, 2008, **61**, 1–39.
15 K. Yu, Z. Wu, Q. Zhao, B. Li and Y. Xie, *J. Phys. Chem. C*, 2008, **112**, 2244–2247.
16 E. Comini, C. Baratto, G. Faglia, M. Ferroni, A. Vomiero and G. Sberveglieri, *Prog. Mater. Sci.*, 2009, **54**, 1–67.
17 J. H. Lee, *Sens. Actuators, B*, 2009, **140**, 319–336.
18 B. Y. Wei, M. C. Hsu, P. G. Su, H. M. Lin, R. J. Wu and H. J. Lai, *Sens. Actuators, B*, 2004, **101**, 81–89.
19 C. Bittencourt, A. Felten, E. H. Espinosa, R. Ionescu, E. Llobet, X. Corteig and J. J. Pireaux, *Sens. Actuators, B*, 2006, **115**, 33–41.
20 C. Balazsi, K. Sedlackova, E. Llobet and R. Ionescu, *Sens. Actuators, B*, 2008, **133**, 151–155.

21 G. H. Lu, L. E. Ocola and J. H. Chen, *Adv. Mater.*, 2009, **21**, 2487–2491.
22 G. Singh, A. Choudhary, D. Haranath, A. G. Joshi, N. Singh, S. Singh and R. Pasricha, *Carbon*, 2012, **50**, 385–394.
23 S. Deng, V. Tjoa, H. M. Fan, H. R. Tan, D. C. Sayle, M. Olivo, S. Mhaisalkar, J. Wei and C. H. Sow, *J. Am. Chem. Soc.*, 2012, **134**, 4905–4917.
24 Q. W. Huang, D. W. Zeng, H. Y. Li and C. S. Xie, *Nanoscale*, 2012, **4**, 5651–5658.
25 P. A. Russo, N. Donato, S. G. Leonardi, S. Baek, D. E. Conte, G. Neri and N. Pinna, *Angew. Chem., Int. Ed.*, 2012, **51**, 11053–11057.
26 S. Srivastava, K. Jain, V. N. Singh, S. Singh, N. Vijayan, N. Dilawar, G. Gupta and T. D. Senguttuvan, *Nanotechnology*, 2012, **23**, 205501.
27 Y. Wang, X. Jiang and Y. Xia, *J. Am. Chem. Soc.*, 2003, **125**, 16176–16177.
28 K. Yong Shin, H. Seung-Chul, K. Kim, H. Yang, C. Sung-Yool, Y. T. Kim, J. T. Park, C. H. Lee, J. Choi, J. Paek and K. Lee, *Appl. Phys. Lett.*, 2005, **86**, 213105.
29 N. Du, H. Zhang, B. D. Chen, X. Y. Ma, Z. H. Liu, J. B. Wu and D. R. Yang, *Adv. Mater.*, 2007, **19**, 1641–1645.
30 J. Su, X.-X. Zou, Y.-C. Zou, G.-D. Li, P.-P. Wang and J.-S. Chen, *Inorg. Chem.*, 2013, **52**, 5924–5930.
31 E. Comini, G. Faglia and G. Sberveglieri, *Sens. Actuators, B*, 2001, **78**, 73–77.
32 S. Mishra, C. Ghanshyam, N. Ram, R. P. Bajpai and R. K. Bedi, *Sens. Actuators, B*, 2004, **97**, 387–390.
33 S. W. Fan, A. K. Srivastava and V. P. Dravid, *Appl. Phys. Lett.*, 2009, **95**, 142106.
34 J. Gong, Y. H. Li, X. S. Chai, Z. S. Hu and Y. L. Deng, *J. Phys. Chem. C*, 2010, **114**, 1293–1298.
35 H. Chen, Y. Liu, C. S. Xie, J. Wu, D. W. Zeng and Y. C. Liao, *Ceram. Int.*, 2012, **38**, 503–509.
36 G. Sakai, N. Matsunaga, K. Shimanoe and N. Yamazoe, *Sens. Actuators, B*, 2001, **80**, 125–131.
37 H. J. Xia, Y. Wang, F. H. Kong, S. R. Wang, B. L. Zhu, X. Z. Guo, J. Zhang, Y. M. Wang and S. H. Wu, *Sens. Actuators, B*, 2008, **134**, 133–139.
38 R. K. Joshi, Q. Hu, F. Am, N. Joshi and A. Kumar, *J. Phys. Chem. C*, 2009, **113**, 16199–16202.
39 J. Zhang, X. H. Liu, S. H. Wu, M. J. Xu, X. Z. Guo and S. R. Wang, *J. Mater. Chem.*, 2010, **20**, 6453–6459.
40 X. H. Liu, J. Zhang, L. W. Wang, T. L. Yang, X. Z. Guo, S. H. Wu and S. R. Wang, *J. Mater. Chem.*, 2011, **21**, 349–356.
41 N. S. Ramgir, I. S. Mulla and K. P. Vijayamohanan, *Sens. Actuators, B*, 2005, **107**, 708–715.
42 K. Jain, R. P. Pant and S. T. Lakshmikumar, *Sens. Actuators, B*, 2006, **113**, 823–829.
43 X. Xu, J. Sun, H. Zhang, Z. Wang, B. Dong, T. Jiang, W. Wang, Z. Li and C. Wang, *Sens. Actuators, B*, 2011, **160**, 858–863.
44 P. Feng, X. Y. Xue, Y. G. Liu, Q. Wan and T. H. Wang, *Appl. Phys. Lett.*, 2006, **89**, 112114.
45 Y. X. Liang, Y. J. Chen and T. H. Wang, *Appl. Phys. Lett.*, 2004, **85**, 666–668.
46 A. C. Patel, S. X. Li, C. Wang, W. J. Zhang and Y. Wei, *Chem. Mater.*, 2007, **19**, 1231–1238.
47 H.-J. Ahn, H.-C. Choi, K.-W. Park, S.-B. Kim and Y.-E. Sung, *J. Phys. Chem. B*, 2004, **108**, 9815–9820.
48 G. Deroubaix and P. Marcus, *Surf. Interface Anal.*, 1992, **18**, 39–46.
49 R. K. Mishra, A. Kushwahab and P. P. Sahay, *RSC Adv.*, 2014, **4**, 3904–3912.
50 D. Kohl, *Sens. Actuators, B*, 1990, **1**, 158–165.
51 M. C. Kung, R. J. Davis and H. H. Kung, *J. Phys. Chem. C*, 2007, **111**, 11767–11775.
52 P. Montmeat, J.-C. Marchand, R. Lalauze, J.-P. Viricelle, G. Tournier and C. Pijolat, *Sens. Actuators, B*, 2003, **95**, 83–89.
53 R. Ludeke, in *Handbook of Surface Science*, ed. K. Horn and M. Scheffler, North-Holland, 2000, pp. 749–862.
54 E. R. Leite, I. T. Weber, E. Longo and J. A. Varela, *Adv. Mater.*, 2000, **12**, 965–968.

